Structure of an endogenous yeast 26S proteasome reveals two major conformational states

Bai Luan (栾白)[a,1], Xiuliang Huang (黄修良)[a,1], Jianping Wu[a], Ziqing Mei[b], Yiwei Wang[a], Xiaobin Xue[a], Chuangye Yan[a], Jiawei Wang[a], Daniel J. Finley[c], Yigong Shi (施一公)[a,2], and Feng Wang (王丰)[a,2]

[a]Ministry of Education Key Laboratory of Protein Science, Tsinghua-Peking Joint Center for Life Sciences, Beijing Advanced Innovation Center for Structural Biology, School of Life Sciences, Tsinghua University, Beijing 100084, China; [b]Biotechnology Research Institute, Chinese Academy of Agricultural Sciences, Beijing 10081, China; and [c]Department of Cell Biology, Harvard Medical School, Boston, MA 02115

Contributed by Yigong Shi, February 4, 2016 (sent for review January 5, 2016; reviewed by Aaron Ciechanover and Huilin Li)

The eukaryotic proteasome mediates degradation of polyubiquitinated proteins. Here we report the single-particle cryoelectron microscopy (cryo-EM) structures of the endogenous 26S proteasome from *Saccharomyces cerevisiae* at 4.6- to 6.3-Å resolution. The fine features of the cryo-EM maps allow modeling of 18 subunits in the regulatory particle and 28 in the core particle. The proteasome exhibits two distinct conformational states, designated M1 and M2, which correspond to those reported previously for the proteasome purified in the presence of ATP-γS and ATP, respectively. These conformations also correspond to those of the proteasome in the presence and absence of exogenous substrate. Structure-guided biochemical analysis reveals enhanced deubiquitylating enzyme activity of Rpn11 upon assembly of the lid. Our structures serve as a molecular basis for mechanistic understanding of proteasome function.

protein degradation | proteasome | cryo-EM | structure

The eukaryotic ubiquitin–proteasome system is responsible for the degradation of polyubiquitinated proteins (1). The 26S proteasome consists of one 20S core particle (CP) and two 19S regulatory particles (RPs). The RP is divided into the lid and base assembly intermediates (1). The lid comprises nine Rpn subunits in yeast (Rpn3/5/6/7/8/9/11/12/15) and the base comprises three Rpn subunits (Rpn1/2/13) and six ATPases (Rpt1–6). Rpn10, which consists of an N-terminal von Willebrand factor A (VWA) domain and multiple C-terminal ubiquitin-interacting motifs (UIM), connects the lid and the base. Polyubiquitin (poly-Ub) chains from substrate are recognized by the RP, leading to unfolding of the substrate and its translocation into the CP, where it is degraded.

The main function of the lid is to remove poly-Ub chains from the substrate (1). The released Ub chains are recycled via further cleavage into Ub monomers. Six of the nine Rpn subunits in the lid (Rpn3/5/6/7/9/12) contain a solenoid fold followed by a proteasome-CSN-eIF3 (PCI) domain of varying lengths; for Rpn8 and Rpn11, each has an Mpr1–Pad1–N-terminal (MPN) domain. Among all Rpn subunits, Rpn11 is the only deubiquitylating enzyme (DUB); it cleaves the isopeptide bond between the carboxyl terminus of Ub and the ε-amino group of Lys in the substrate (2, 3). Except for Rpn15/Sem1/Dss1, the C-terminal sequences of the other eight Rpn subunits in the lid form a helix bundle, which dictates lid assembly (4, 5).

In the base, the six Rpt subunits form a hexameric ring. Powered by ATP hydrolysis, the Rpt ring is responsible for substrate unfolding and translocation of the unfolded substrate through the narrow RP central channel into the CP for degradation (6–8). The barrel-shaped CP consists of two outer α-rings and two inner β-rings, each containing seven subunits (α1–7 or β1–7). X-ray structures of the CP at atomic resolution have been reported for archaeabacteria (9), yeast (10), and mammals (11).

Crystallization of the RP or the 26S proteasome is hampered by its dynamic nature. Improvement of cryo-EM technologies has allowed structural determination of the proteasome at varying resolutions (8, 12–18). Eight Rpn subunits were identified in the lid by cryo-EM analysis of the proteasome from *Saccharomyces cerevisiae* (*S. cerevisiae*) (8) and *Schizosaccharomyces pombe* (*S. pombe*) (12). The cryo-EM structure of an intact proteasome from *S. cerevisiae* was determined at 7.4-Å resolution, which allowed identification and modeling of all RP subunits (13, 19). These advances were followed by identification of distinct conformational states of the proteasome (15–17). In this manuscript, we report the cryo-EM structures of the *S. cerevisiae* 26S proteasome at improved resolutions, describe important structural features, and identify two distinct conformational states of the proteasome that are shared with other reported structures.

Results

Sample Preparation and Electron Microscopy. Following a published protocol (20), we purified the *S. cerevisiae* proteasome. Approximately 3.3 mg purified sample was obtained from a 12-L culture (Fig. S1 *A* and *B*). Analysis of the purified sample by native PAGE revealed two major species of 2:1 and 1:1 stoichiometry between the RP and CP (Fig. S1*C*, lane 1). Incubation of the native PAGE gel with the fluorogenic substrate Sucrose-Leu-Leu-Val-Try-7-Amido-4-Methylcoumarin (Suc-LLVY-AMC) confirmed the proteolytic activity of the two proteasomal species (Fig. S1*C*, lane 2).

The purified proteasome was imaged on a Titan Krios electron microscope (Fig. S1*D*); 183,626 particles were semiautopicked from 5,517 micrographs. After reference-free two-dimensional (2D) classification (Fig. S1*E*), 166,564 particles were subjected to three-dimensional (3D) refinement, followed by 3D classification with a mask on the CP and one RP (Fig. S2*A*); 81,782 particles from two classes and 25,151 particles from another class were

Significance

Mechanistic understanding of proteasome function requires elucidation of its three-dimensional structure. Previous investigations have revealed increasingly detailed information on the overall organization of the yeast 26S proteasome. In this study, we further improved the resolution of cryo-EM structures of endogenous proteasomes from *Saccharomyces cerevisiae*. These structures reveal two distinct conformational states, which appear to correspond to different states of ATP hydrolysis and substrate binding. This information may guide future functional analysis of the proteasome.

Author contributions: B.L., X.H., Y.S., and F.W. designed research; B.L., X.H., J. Wu, Z.M., Y.W., X.X., and F.W. performed research; B.L., X.H., J. Wu, C.Y., J. Wang, D.J.F., Y.S., and F.W. analyzed data; and B.L., X.H., J. Wu, D.J.F., Y.S., and F.W. wrote the paper.

Reviewers: A.C., Technion–Israel Institute of Technology; and H.L., Stony Brook University.

The authors declare no conflict of interest.

Freely available online through the PNAS open access option.

Data deposition: The atomic coordinates of the M1 and M2 conformations have been deposited in the Protein Data Bank, www.pdb.org (PDB ID codes 3JCO and 3JCP, respectively). The cryo-EM maps have been deposited in the EMDataBank, www.emdatabank.org (accession nos. EMD-6574 through EMD-6579).

[1]B.L. and X.H. contributed equally to this work.

[2]To whom correspondence may be addressed. Email: shi-lab@tsinghua.edu.cn or wfeng@tsinghua.edu.cn.

This article contains supporting information online at www.pnas.org/lookup/suppl/doi:10.1073/pnas.1601561113/-/DCSupplemental.

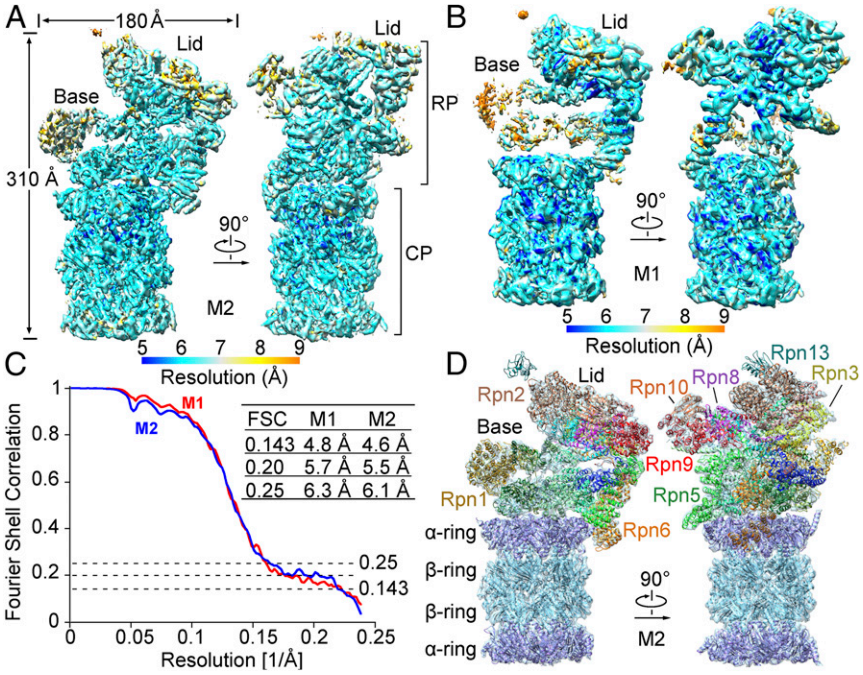

Fig. 1. Cryo-EM structure of the *S. cerevisiae* proteasome. (*A*) Overall cryo-EM map of the proteasome from *S. cerevisiae* in the M2 conformational state. The average resolution is 4.6 and 6.1 Å on the basis of FSC values of 0.143 and 0.25, respectively. The range of resolution is color-coded below the maps. (*B*) Overall cryo-EM map of the proteasome in the M1 conformational state. The cryo-EM maps in the M1 state are poorer in the base than those in the M2 state. (*C*) FSC curves of the cryo-EM reconstructions. Depending on the FSC values chosen, the resolutions for these two structures range between 4.6 and 6.3 Å. (*D*) Overall structure of the proteasome. A near-complete model for the backbone was built to fit the cryo-EM maps. Structural images in Figs. 1, 3*A*, 4, and 5*C* were prepared using Chimera (33). Images in Figs. 2, 3 *B–L*, and 5*B* were made in PyMOL (35).

subjected to an autorefine subroutine. These two reconstructions may represent distinct conformations of the proteasome, designated the M1 and M2 states (Fig. S2 *B* and *C*). The final cryo-EM maps for the M1 and M2 states have overall resolutions of 4.8 and 4.6 Å, respectively, on the basis of the gold-standard Fourier shell correlation (FSC) value of 0.143 (Fig. 1 *A–C*). For both reconstructions, the FSC curves shift to the right around 5–6 Å, and thus may yield inflated resolutions (Fig. 1*C*). The overall resolutions for the M1 and M2 states are adjusted to 6.3 and 6.1 Å, respectively, based on the FSC value of 0.25.

We also imaged the sample on a Tecnai Arctica microscope (Fig. S3); 133,198 particles from one class and 16,063 particles from another were autorefined to yield the M1 and M2 reconstructions with overall resolutions of 5.8 and 8.3 Å, respectively, on the basis of the FSC gold standard (Figs. S3 and S4 *A–D*). The M1 and M2 structures determined on the Tecnai Arctica microscope exhibit features nearly identical to those on the Titan Krios (Fig. S4 *E* and *F*). For simplicity, we focus our discussion on the structures derived from the Titan Krios.

Structure of the *S. cerevisiae* Proteasome. The final cryo-EM maps of the proteasome exhibit clear overall features, with most secondary structural elements identifiable (Fig. 1 *A* and *B*). With one RP counted, the proteasome measures 310 Å in length and 180 Å across the RP at its widest point (Fig. 1*A*). For the M2 state, 12 Rpn and 6 Rpt subunits exhibit decent cryo-EM density and can be unambiguously assigned (Figs. S5 and S6). The only exception is the distally located Ub receptor Rpn13, which displays poor EM density (Fig. 1 *A* and *D*). A large cavity is created between the lid and the Rpt subunits, with Rpn1 on the side (Fig. 1*D* and Fig. S6*A*). Compared with reported structures (8, 13, 15, 17), the cryo-EM map of the M2 state exhibits improved overall and local features. The Rpn subunits in the lid, Rpn1, and Rpt subunits display improved features for the α-helices (Fig. S7). A coiled-coil of two α-helices between Rpt1 and Rpt2 in our structure, as opposed to a single α-helix from Rpt1 (17), is found to directly bind Rpn1 (Fig. S7*C*). A near-complete model of the Cα trace was built for the M2 state (Fig. 1*D* and Table S1). The general features are similar to those reported previously (8, 13, 15, 17).

The lid resembles an open hand (Fig. 2*A*). The solenoid folds of Rpn3 and Rpn12 closely associate with each other, forming the thumb; the solenoid folds of the other four subunits Rpn7, Rpn6, Rpn5, and Rpn9 correspond to the index, middle, ring, and little fingers, respectively. The palm is formed by the PCI domains of these Rpn subunits. Notably, the N termini of these six Rpn subunits are placed at the tips of the five fingers, with their C-terminal α-helices forming two end-to-end stacked bundles in

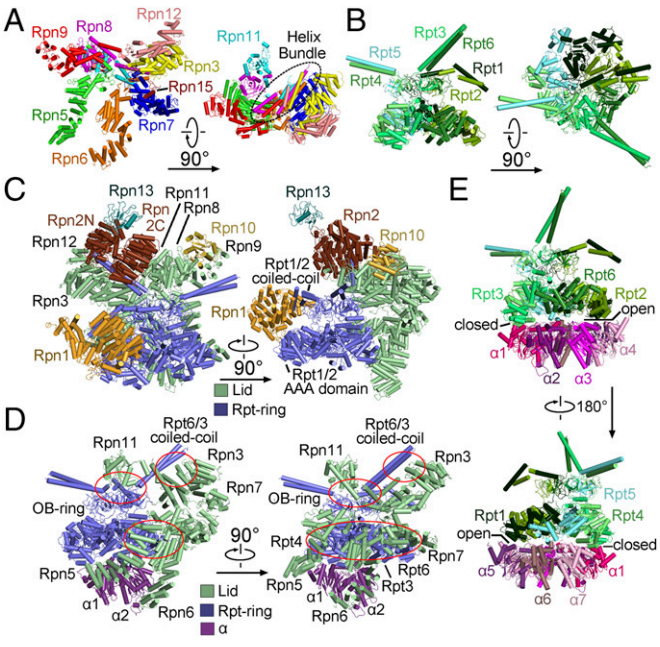

Fig. 2. Structural organization of the RP. (*A*) Overall structure of the lid. The open-hand structure of the lid is shown in two perpendicular views. The C-terminal helix bundle is highlighted by a dashed oval circle. (*B*) The two-layered structure of the Rpt ring. (*C*) The spatial arrangement of Rpn1, Rpn2, Rpn10, and Rpn13, relative to the lid (pale green) and the Rpt ring (slate). (*D*) Three discrete interfaces between the lid and the Rpt ring. The interfaces are identified by red ovals. (*E*) Asymmetric interactions between the hexameric Rpt ring and the heptameric CP ring. The loose and tight interactions between the Rpt ring and the α-ring are indicated as "open" and "closed," respectively.

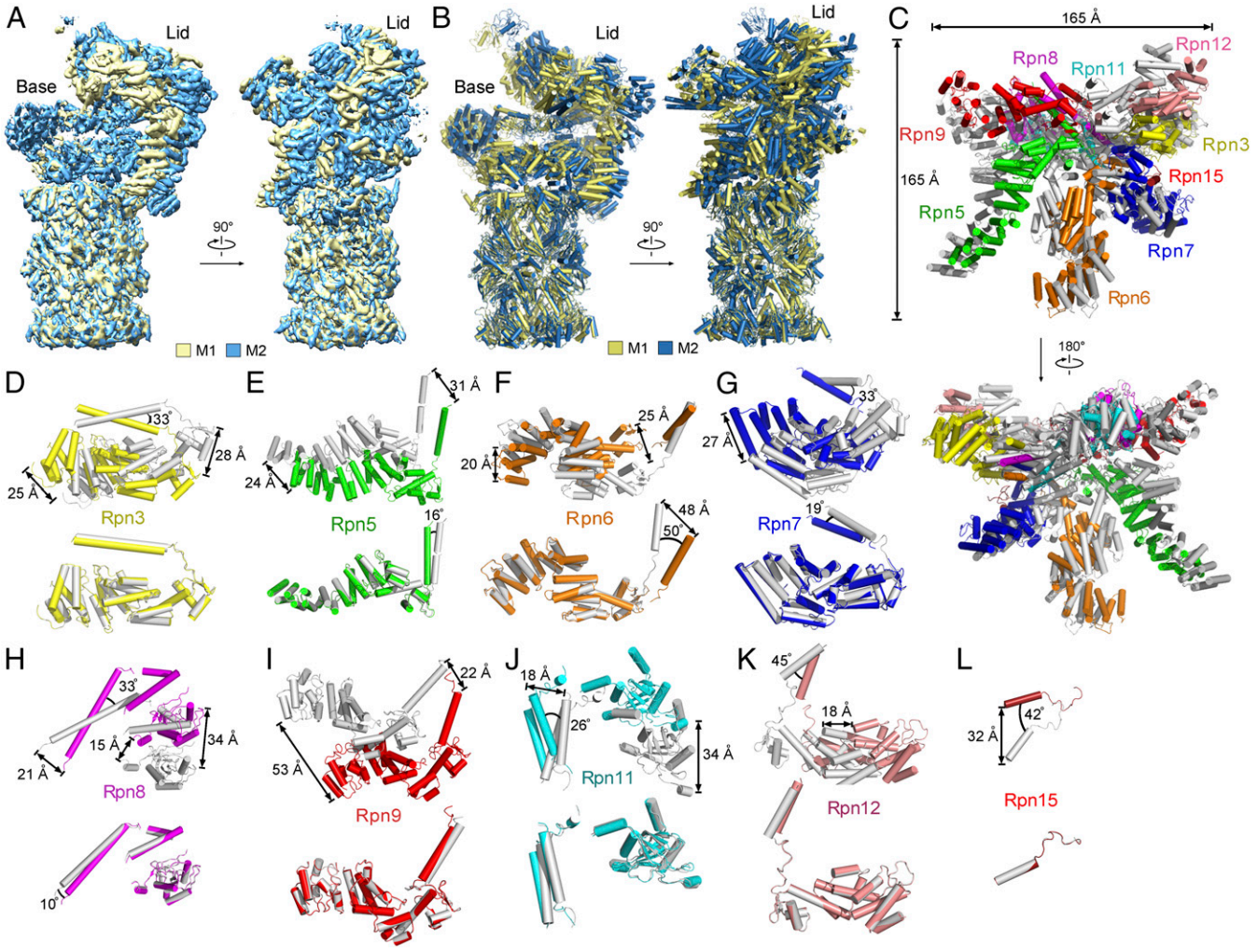

Fig. 3. Structural comparison of the two conformational states. (*A*) Comparison of the cryo-EM maps between the M1 and M2 states. The cryo-EM maps are colored yellow and cyan for the M1 and M2 states, respectively. Relative to the CP, the RP displays pronounced conformational differences for the two states. (*B*) Comparison of the structural models between the M1 and M2 states. (*C*) Comparison of the lid in the two states. The Rpn subunits in the M1 and M2 states are shown in gray and coded by color, respectively. (*D*) Rpn3 in the two states exhibits large variations (*Upper*) but can be aligned to each other (*Lower*). The two structures of Rpn3 (*Upper*) are taken directly from *C*. The other eight Rpn subunits are similarly compared in *E*–*L*, with conformational variations (*Upper*) and aligned structures (*Lower*) shown. These eight Rpn subunits are Rpn5 (*E*), Rpn6 (*F*), Rpn7 (*G*), Rpn8 (*H*), Rpn9 (*I*), Rpn11 (*J*), Rpn12 (*K*), and Rpn15 (*L*).

the palm (Fig. 2*A*). The intrinsic DUB Rpn11 interacts with Rpn8 above the palm, next to the C-terminal helix bundle. This arrangement places Rpn11 in the center of the lid yet makes it accessible to incoming poly-Ub chains (Fig. 2*A* and Fig. S6*A*). For the smallest proteasomal subunit Rpn15, only the C-terminal helix and an extended loop are assigned. The helix binds the solenoid of Rpn7, whereas the loop stretches toward Rpn3, suggesting an interaction between the N-terminal portion of Rpn15 and Rpn3 as predicted (19, 21).

Each Rpt subunit sequentially consists of an N-terminal helical domain, oligonucleotide/oligosaccharide-binding (OB) domain, and ATPase associated with diverse cellular activities (AAA) domain. The six Rpt subunits in the order of Rpt1-2-6-3-4-5 assemble into a two-layered structure, with six OB domains forming a small ring above the AAA ring (Fig. 2*B*). The N-terminal helical domains of these Rpt subunits form three coiled-coils: Rpt1/2, Rpt6/3, and Rpt4/5. The Rpt1/2 coiled-coil interacts with Rpn1, whereas Rpn1 lies at the edge of the Rpt ring and interacts with the AAA domains of Rpt1 and Rpt2 (Fig. 2*C*). The Rpt6/3 coiled-coil extends out to the C-terminal helical bundle of the lid and interacts with Rpn2, which is located at the top of the Rpt ring (Fig. 2*C*). Notably, the Rpt4/5 coiled-coil projects out in isolation and makes no contact with other subunits.

The lid directly contacts the Rpt ring through three discrete interfaces (Fig. 2*D*). One interface involves the N-terminal solenoids of Rpn5, Rpn6, and Rpn7, which interact with Rpt4, Rpt3, and Rpt6, respectively, on the periphery of the AAA ring. The solenoid fold of Rpn6 extends further to the CP, making close interactions with the α2-subunit; the solenoid fold of Rpn5 also directly contacts α1 (Fig. 2*D*). Another interface involves the MPN domain of Rpn11 and the OB ring in the center of the lid. The third interface is mediated by Rpn3 and the coiled-coil of Rpt6/Rpt3.

Although Rpn1, Rpn2, and Rpn13 are assigned to the base, they are spatially separated from each other (Fig. 2*C*). Rpn1 makes no contact with the lid or other Rpn subunits, providing an explanation for the highly flexible nature of Rpn1 within the proteasome. In addition to binding the coiled-coil of Rpt6/Rpt3, the N-terminal helices of Rpn2 contact Rpn3 and Rpn12 whereas its C-terminal helices interact with Rpn11. The N-terminal VWA domain of Rpn10 is located at the top edge of the RP, making contacts with Rpn8 and Rpn9. The ubiquitin-binding UIM of Rpn10 was invisible. Rpn13 only binds Rpn2 at the apical end of the proteasome.

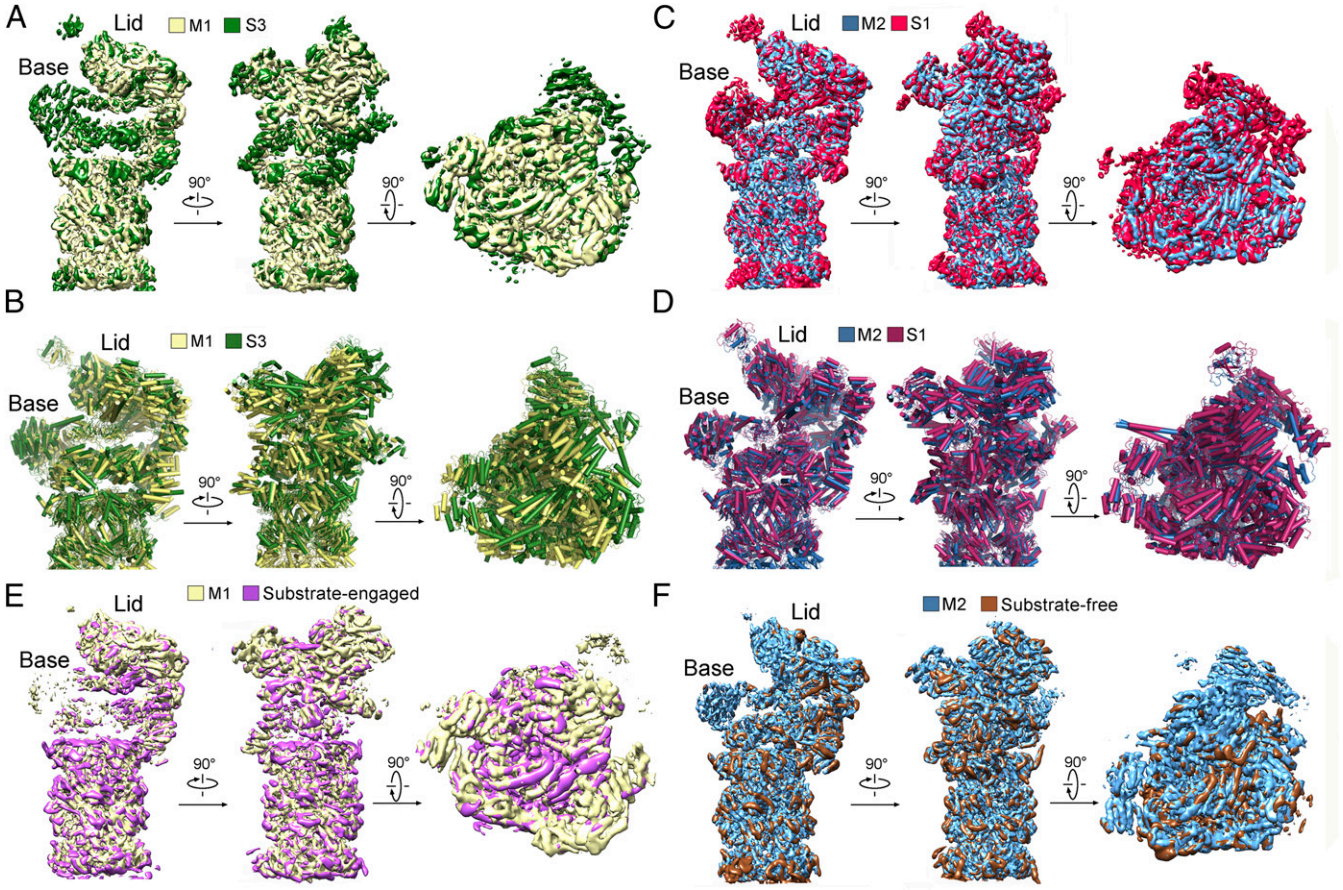

Fig. 4. M1 and M2 conformational states are similar to those reported earlier. (*A*) The M1 state is similar to the S3 state (17). Shown here is a comparison of the cryo-EM maps. (*B*) Structural overlay between the M1 and S3 states. (*C*) The M2 state is similar to the S1 state (17). Shown here is a comparison of the cryo-EM maps. (*D*) Structural overlay between the M2 and S1 states. (*E*) The M1 state is similar to the reported substrate-engaged state (15). (*F*) The M2 state is similar to the reported substrate-free state (15).

In addition to Rpn6 binding to the α2-subunit, the RP is connected to the CP through asymmetric interactions between the hexameric Rpt ring and the heptameric CP ring (Fig. 2*E*). Specifically, the AAA domains of Rpt4 and Rpt5 closely stack against the α1/7- and α6/7-subunits, respectively. Compared with these close interactions, the Rpt2/6 end of the Rpt ring is slightly separated from the α-ring. The C-terminal tails of a subset of Rpt subunits are thought to bind the α-pockets at the interfaces between neighboring α-subunits. These interactions may anchor the RP to the CP as well as signal the opening of the CP gate. Unfortunately, there is little cryo-EM density for these Rpt C-terminal tails in our structure.

Comparison Between the M1 and M2 States. For the M1 state, the Rpn subunits are well-defined; however, the six Rpt subunits in the base exhibit discontinuous cryo-EM density (Fig. 1*B*), likely due to their dynamic conformational states associated with ATP binding and hydrolysis. Comparison of the cryo-EM maps between the M1 and M2 states reveals pronounced structural differences in the RP but not in the CP (Fig. 3*A*). The major differences reflect significant movement and rotation of most Rpn and Rpt subunits in the RP relative to the CP (Fig. 3*B* and Fig. S4*D*). The lid as a whole shows no obvious directionality in movement.

In the lid, all nine Rpn subunits exhibit different conformations between the two states (Fig. 3*C*). Rpn3 subunits in the two states are related to each other by a 33° rigid-body rotation, resulting in separation of up to 25–28 Å at the periphery (Fig. 3*D*, *Upper*); these two subunits can be superimposed with a root-mean-square deviation (rmsd) of 0.44 Å (Fig. 3*D*, *Lower*). Rpn5 subunits in the two states, separated by 24–31 Å, can be aligned with an rmsd of 0.42 Å for 372 Cα atoms (Fig. 3*E*). The other seven Rpn subunits each displays a set of distinct structural differences (Fig. 3 *F*–*L*). Altogether, for five of the nine Rpn subunits (Rpn3/9/11/12/15), structures in the M1 and M2 states can be superimposed very well, suggesting rigid-body movement. For the other four subunits (Rpn5/6/7/8), such superposition brings the solenoid folds and PCI domains into good registry, but not the C-terminal helices (Fig. 3 *E*–*H*).

Comparison with Published Structures of the Proteasome. Comparison with published structures suggests that the M1 and M2 states may correspond to those of the proteasome determined in the presence of ATP-γS and ATP, respectively (17). The cryo-EM map of the M1 state exhibits similar structural features as those of the S3 state (17) (Fig. 4*A*). The majority of the secondary structural elements in the M1 state are aligned with those in the S3 state, with an overall rmsd of 2.02 Å (Fig. 4*B*). The cryo-EM map of the M2 state resembles that of the S1 state (Fig. 4*C* and Fig. S8*A*), which was determined in the presence of ATP (17); their backbone models are superimposed with an rmsd of 1.71 Å (Fig. 4*D*). Nonetheless, the overall resemblance applies to the individual subunits but not necessarily to every secondary structural element. The M1 and M2 states of the proteasome are also reminiscent of the substrate-engaged and substrate-free states, respectively (15) (Fig. 4 *E* and *F* and Fig. S8*B*). A direct inference from this analysis is that the presence of ATP-γS, or the absence of ATP hydrolysis, may correlate with substrate

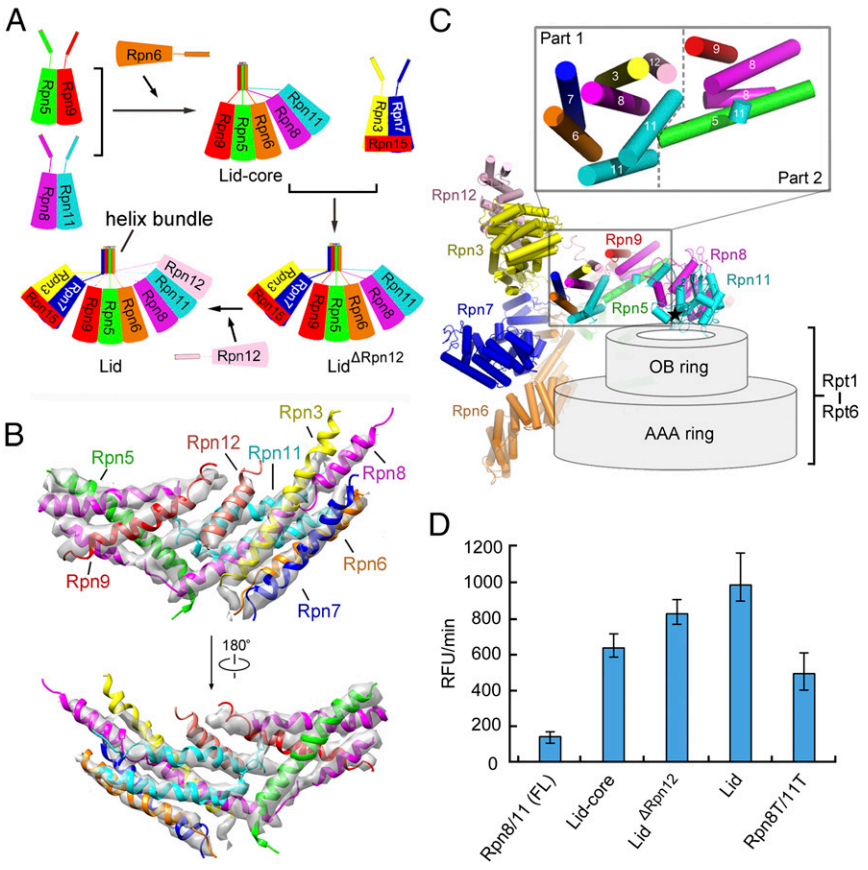

Fig. 5. DUB activity of Rpn11 is markedly increased along with assembly of the lid. (*A*) A schematic diagram for the assembly of the lid. The C-terminal helices of the Rpn subunits are thought to facilitate the assembly by forming a helix bundle. (*B*) The cryo-EM maps of the C-terminal helix bundle in the lid. (*C*) Spatial arrangement of the Rpn subunits in the lid relative to the hexameric Rpt ring. A close-up view of the C-terminal helix bundle in the lid is shown. The catalytic site of Rpn11 is indicated by a black asterisk, which is positioned right above the pore of the OB ring. (*D*) The DUB activity of Rpn11 is markedly increased along with the assembly of the lid, as measured by cleavage of the fluorogenic substrate Ub-AMC. Rpn8T/11T denotes the heterodimer Rpn8 (residues 1–178)–Rpn11 (residues 1–239). SDs are calculated from three independent experiments. FL, full-length; RFU, relative fluorescence units.

binding. This analysis suggests that mutational loss of ATPase activity, but not ATP binding, may facilitate substrate association, which can be experimentally tested.

Regulation of the DUB Activity of Rpn11. The RP recycles the poly-Ub chain through the intrinsic DUB activity of Rpn11 in the lid. Rpn8 is a catalytically inactive paralog of Rpn11 and forms a stable heterodimer with Rpn11 (22, 23) (Fig. 5*A* and Fig. S9*A*). Assembly of the lid is believed to occur in a hierarchical fashion (5, 24–26) (Fig. 5*A*), primarily driven by formation of the C-terminal helix bundle that includes domains from Rpn3/5/6/7/8/9/11/12 (4, 5). In our structure, the α-helices in the bundle are clearly defined (Fig. 5*B*), and the bundle is spatially divided into two stacked portions (Fig. 5 *B* and *C*). Part 1 contains seven α-helices from Rpn3/6/7/8/11/12, where two helices come from Rpn11. Part 2 consists of five α-helices from Rpn5/8/9/11, including two from Rpn8.

The full-length Rpn8–11 dimer had little DUB activity, and truncation of the C-terminal sequences in Rpn8–11 led to marked elevation of the DUB activity (22, 23). In our structure, the active site of Rpn11 is separated from the C-terminal helices by a distance of ∼44 Å (Fig. S9*A*). Thus, the DUB activity of the lid is unlikely to be directly inhibited by the C-terminal helices in the assembled lid.

To examine the relationship between the DUB activity of Rpn11 and assembly of the lid, we expressed and purified five distinct Rpn11-containing complexes, including the full-length Rpn8–11, truncated Rpn8–11, core subunits of the lid (lid-core; Rpn5/6/8/9/11), lid without the subunit Rpn12 (lid$^{\Delta Rpn12}$), and lid (Fig. S9 *B–D*). These bacterially expressed complexes represent distinct stages of the lid formation. First, the DUB activity was qualitatively assessed using Lys48-linked diubiquitin (Lys48-Ub_2) (Fig. S9 *E–I*). All Rpn8–11–containing complexes are able to cleave Lys48-Ub_2, with the full-length Rpn8–11 complex displaying the lowest activity. The intact lid seems to be more active compared with lid-core or lid$^{\Delta Rpn12}$. Two missense mutations (H109A, H111A) were introduced into the catalytic residues to abolish the DUB activity of Rpn11, generating a catalytically inactive lid (lid^{AXA}) (2, 3) (Fig. S9*I*).

Next, we reconstituted an in vitro assay using the fluorogenic substrate Ub-AMC. The full-length Rpn8–11 complex exhibits a basal-level DUB activity (Fig. 5*D*). This activity was enhanced by about fivefold for lid-core, sixfold for lid$^{\Delta Rpn12}$, and sevenfold for the intact lid. These results support the conclusion that the DUB activity increases along with the stepwise assembly of the lid. Consistent with published studies (22, 23), truncation of the C-terminal helices in Rpn8–11 also results in higher DUB activity, but this activity is lower than that of the lid-core (Fig. 5*D*). Thus, the increased DUB activity may be associated not just with the relief of steric hindrance from the C-terminal helices but also with assembly of the lid. Interactions with other Rpn subunits may bring activating conformational changes to Rpn11 or enhance substrate recruitment and targeting.

Discussion

In this study, we report the cryo-EM structures of the *S. cerevisiae* proteasome at resolutions of 4.6–6.3 Å. As anticipated, the cryo-EM density in the CP is generally better-resolved than that in the RP. Within the RP, the cryo-EM density in the lid is better-resolved over that in the base, especially the Rpt ring. This is likely caused by the heterogeneous conformation of the six Rpt subunits, each of which may exhibit three distinct states: ATP-bound, ADP-bound, and nucleotide-free. Combination of the various states among the six Rpt subunits generates a large number of conformations for the Rpt ring. Such heterogeneity may indirectly affect the Rpn subunits in the RP, thus hindering improvement of the overall resolution.

Data collected on two different microscopes both yielded two distinct conformational states of the proteasome. Intriguingly,

the M1/M2 states correspond to those determined in the presence of ATP-γS/ATP (17) or in the presence/absence of exogenous substrate (15). Unlike the earlier studies, no ATP-γS or exogenous substrate was added to our sample preparation, and the Rpt and Rpn subunits contain no mutation. Only Rpn11 is N-terminally tagged with protein A, which is removed during proteasome purification. Our approach involves minimal alteration to the proteasomal subunits and ensures that the resulting proteasome is as native as possible. This analysis argues that the M1 and M2 states likely reflect physiologically populated conformations of the proteasome.

Despite obvious movement and rotation of individual Rpn/Rpt subunits in the RP between the M1 and M2 states, the distance between the two ubiquitin receptors Rpn10 and Rpn13 remains largely unchanged. This observation supports a conserved mode of poly-Ub chain recognition by the proteasome. The minimal number of Ubs in a poly-Ub chain for faithful recognition by the proteasome is four (27), and the space between Rpn10 and Rpn13 is thought to be appropriate for the accommodation of a tetra-Ub chain (8, 27, 28).

Few changes are seen in Rpn8 and Rpn11 when the structure of the C-terminally truncated Rpn8–11 complex (22, 23) is compared with that in the proteasome. Assuming that the structure of the assembled lid is the same as that in the proteasome, this observation indicates that the C-terminal helices of Rpn8 and Rpn11 indeed inhibit the DUB activity of Rpn11. This inhibition might be beneficial to cells, because it would avoid promiscuous deubiquitination before assembly of the lid. While this manuscript was under review, the cryo-EM structure of a recombinant lid at 3.5-Å resolution was published, which reveals fine features of nine Rpn subunits (29).

Materials and Methods

The *S. cerevisiae* strain sMK50 (30) was used for proteasome purification. The purified 26S proteasomes were imaged by an FEI Falcon II direct electron detector mounted on an FEI Titan Krios electron microscope operating at 300 kV and an FEI Tecnai Arctica electron microscope operating at 200 kV. Image processing was performed in RELION 1.4 (31). Model building and refinement were performed in Coot (32), Chimera (33), and PHENIX (34). The images of cryo-EM maps and models were prepared using Chimera (33) and PyMOL (35). The atomic coordinates of the M1 and M2 conformations of the yeast 26S proteasome have been deposited in the Protein Data Bank under ID codes 3JCO and 3JCP, respectively. The cryo-EM maps have been deposited in the EMDataBank under accession nos. EMD-6574 through EMD-6579.

ACKNOWLEDGMENTS. We thank the Tsinghua University Branch of the China National Center for Protein Sciences (Beijing) for providing facility support. This work was supported by National Natural Science Foundation of China Grants 31321062 and 31430020 (to Y.S.), 31100524 (to Z.M.), and 31270764 (to F.W.), and NIH Grant R37-GM043601 (to D.J.F.).

1. Finley D, Chen X, Walters KJ (2016) Gates, channels, and switches: Elements of the proteasome machine. *Trends Biochem Sci* 41(1):77–93.
2. Yao T, Cohen RE (2002) A cryptic protease couples deubiquitination and degradation by the proteasome. *Nature* 419(6905):403–407.
3. Verma R, et al. (2002) Role of Rpn11 metalloprotease in deubiquitination and degradation by the 26S proteasome. *Science* 298(5593):611–615.
4. Estrin E, Lopez-Blanco JR, Chacón P, Martin A (2013) Formation of an intricate helical bundle dictates the assembly of the 26S proteasome lid. *Structure* 21(9):1624–1635.
5. Tomko RJ, Jr, et al. (2015) A single α helix drives extensive remodeling of the proteasome lid and completion of regulatory particle assembly. *Cell* 163(2):432–444.
6. Zhang F, et al. (2009) Structural insights into the regulatory particle of the proteasome from *Methanocaldococcus jannaschii*. *Mol Cell* 34(4):473–484.
7. Wang F, et al. (2011) Structure and mechanism of the hexameric MecA-ClpC molecular machine. *Nature* 471(7338):331–335.
8. Lander GC, et al. (2012) Complete subunit architecture of the proteasome regulatory particle. *Nature* 482(7384):186–191.
9. Löwe J, et al. (1995) Crystal structure of the 20S proteasome from the archaeon *T. acidophilum* at 3.4 Å resolution. *Science* 268(5210):533–539.
10. Groll M, et al. (1997) Structure of 20S proteasome from yeast at 2.4 Å resolution. *Nature* 386(6624):463–471.
11. Unno M, et al. (2002) The structure of the mammalian 20S proteasome at 2.75 Å resolution. *Structure* 10(5):609–618.
12. Lasker K, et al. (2012) Molecular architecture of the 26S proteasome holocomplex determined by an integrative approach. *Proc Natl Acad Sci USA* 109(5):1380–1387.
13. Beck F, et al. (2012) Near-atomic resolution structural model of the yeast 26S proteasome. *Proc Natl Acad Sci USA* 109(37):14870–14875.
14. da Fonseca PC, He J, Morris EP (2012) Molecular model of the human 26S proteasome. *Mol Cell* 46(1):54–66.
15. Matyskiela ME, Lander GC, Martin A (2013) Conformational switching of the 26S proteasome enables substrate degradation. *Nat Struct Mol Biol* 20(7):781–788.
16. Śledź P, et al. (2013) Structure of the 26S proteasome with ATP-γS bound provides insights into the mechanism of nucleotide-dependent substrate translocation. *Proc Natl Acad Sci USA* 110(18):7264–7269.
17. Unverdorben P, et al. (2014) Deep classification of a large cryo-EM dataset defines the conformational landscape of the 26S proteasome. *Proc Natl Acad Sci USA* 111(15):5544–5549.
18. Aufderheide A, et al. (2015) Structural characterization of the interaction of Ubp6 with the 26S proteasome. *Proc Natl Acad Sci USA* 112(28):8626–8631.
19. Bohn S, et al. (2013) Localization of the regulatory particle subunit Sem1 in the 26S proteasome. *Biochem Biophys Res Commun* 435(2):250–254.
20. Leggett DS, Glickman MH, Finley D (2005) Purification of proteasomes, proteasome subcomplexes, and proteasome-associated proteins from budding yeast. *Methods Mol Biol* 301:57–70.
21. Tomko RJ, Jr, Hochstrasser M (2014) The intrinsically disordered Sem1 protein functions as a molecular tether during proteasome lid biogenesis. *Mol Cell* 53(3):433–443.
22. Pathare GR, et al. (2014) Crystal structure of the proteasomal deubiquitylation module Rpn8-Rpn11. *Proc Natl Acad Sci USA* 111(8):2984–2989.
23. Worden EJ, Padovani C, Martin A (2014) Structure of the Rpn11-Rpn8 dimer reveals mechanisms of substrate deubiquitination during proteasomal degradation. *Nat Struct Mol Biol* 21(3):220–227.
24. Sharon M, Taverner T, Ambroggio XI, Deshaies RJ, Robinson CV (2006) Structural organization of the 19S proteasome lid: Insights from MS of intact complexes. *PLoS Biol* 4(8):e267.
25. Isono E, et al. (2007) The assembly pathway of the 19S regulatory particle of the yeast 26S proteasome. *Mol Biol Cell* 18(2):569–580.
26. Fukunaga K, Kudo T, Toh-e A, Tanaka K, Saeki Y (2010) Dissection of the assembly pathway of the proteasome lid in *Saccharomyces cerevisiae*. *Biochem Biophys Res Commun* 396(4):1048–1053.
27. Thrower JS, Hoffman L, Rechsteiner M, Pickart CM (2000) Recognition of the polyubiquitin proteolytic signal. *EMBO J* 19(1):94–102.
28. Sakata E, et al. (2012) Localization of the proteasomal ubiquitin receptors Rpn10 and Rpn13 by electron cryomicroscopy. *Proc Natl Acad Sci USA* 109(5):1479–1484.
29. Dambacher CM, Worden EJ, Herzik MA, Jr, Martin A, Lander GC (2016) Atomic structure of the 26S proteasome lid reveals the mechanism of deubiquitinase inhibition. *eLife* 5:e13027.
30. Kleijnen MF, et al. (2007) Stability of the proteasome can be regulated allosterically through engagement of its proteolytic active sites. *Nat Struct Mol Biol* 14(12):1180–1188.
31. Scheres SH (2012) RELION: Implementation of a Bayesian approach to cryo-EM structure determination. *J Struct Biol* 180(3):519–530.
32. Emsley P, Cowtan K (2004) Coot: Model-building tools for molecular graphics. *Acta Crystallogr D Biol Crystallogr* 60(Pt 12 Pt 1):2126–2132.
33. Pettersen EF, et al. (2004) UCSF Chimera—A visualization system for exploratory research and analysis. *J Comput Chem* 25(13):1605–1612.
34. Adams PD, et al. (2002) PHENIX: Building new software for automated crystallographic structure determination. *Acta Crystallogr D Biol Crystallogr* 58(Pt 11):1948–1954.
35. DeLano WL (2002) The PyMOL Molecular Graphics System. Available at www.pymol.org.
36. Dong KC, et al. (2011) Preparation of distinct ubiquitin chain reagents of high purity and yield. *Structure* 19(8):1053–1063.
37. Li X, et al. (2013) Electron counting and beam-induced motion correction enable near-atomic-resolution single-particle cryo-EM. *Nat Methods* 10(6):584–590.
38. Mindell JA, Grigorieff N (2003) Accurate determination of local defocus and specimen tilt in electron microscopy. *J Struct Biol* 142(3):334–347.
39. Chen S, et al. (2013) High-resolution noise substitution to measure overfitting and validate resolution in 3D structure determination by single particle electron cryomicroscopy. *Ultramicroscopy* 135:24–35.
40. Kucukelbir A, Sigworth FJ, Tagare HD (2014) Quantifying the local resolution of cryo-EM density maps. *Nat Methods* 11(1):63–65.